

# Getting the electrons right for O2-on-metal systems Bree, R.A.B. van

#### Citation

Bree, R. A. B. van. (2025, October 21). *Getting the electrons right for O2-on-metal systems*. Retrieved from https://hdl.handle.net/1887/4279459

Version: Publisher's Version

Licence agreement concerning inclusion of doctoral

License: thesis in the Institutional Repository of the University of

<u>Leiden</u>

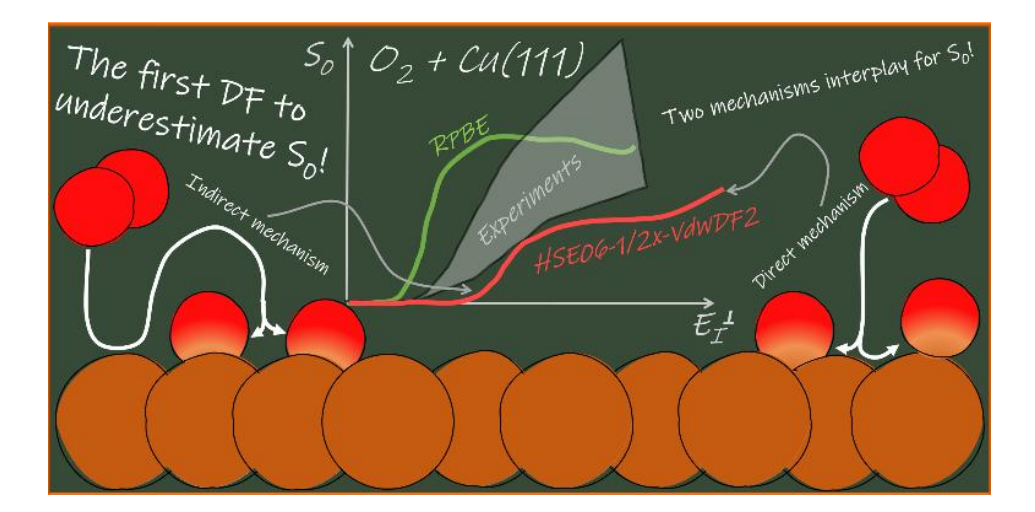
Downloaded from: <a href="https://hdl.handle.net/1887/4279459">https://hdl.handle.net/1887/4279459</a>

**Note:** To cite this publication please use the final published version (if applicable).

# 5 O<sub>2</sub> dissociation on Cu(111): Dynamics on a novel screened hybrid Van der Waals DFT potential energy surface

#### This chapter is based on:

van Bree, R. A. B.; Kroes, G. J. O<sub>2</sub> Dissociation on Cu(111) Dynamics on a Novel Screened Hybrid Van der Waals DFT Potential Energy Surface. *J. Phys. Chem. C* **2024**, *128* (45), 19182–19196. https://doi.org/10.1021/acs.jpcc.4c05466.



## **Abstract**

The dissociative chemisorption (DC) of  $O_2$  on Cu(111) has been extensively studied by both theory and experiment. Different experiments disagree on the underlying mechanisms (direct or indirect) for the sticking of  $O_2$ . Thus far, studies based on density functional theory (DFT) favour the indirect mechanism. However, DFT has not fully resolved the discussion, as DFT based on the generalised gradient approximation (GGA) has always substantially overestimated the reactivity and sticking probabilities of  $O_2$  on Cu(111) and other Cu surfaces. Recent work indicated that this overestimation is due to the failure of GGA DFT to describe molecule-metal systems where the charge transfer energy ( $E_{CT}$ ), i.e., the work function of the metal surface minus the electron affinity of the molecule, is below  $7 \, eV$ .  $O_2 + Cu(111)$  is one such system. This chapter presents computed sticking probabilities for  $O_2 + Cu(111)$  based on

the HSE06-1/2x-VdWDF2 screened hybrid Van der Waals density functional (DF), which is applied self-consistently. A six-dimensional static surface potential energy surface (PES) was constructed using the corrugation-reducing procedure. This PES was used to perform quasi-classical trajectory calculations to compute the sticking probabilities of  $O_2$  + Cu(111). For the first time, we present DFTbased sticking probabilities that underestimate the experimental sticking probabilities. While reproducing the experimental results would have been even more desirable the fact that we found a DF which underestimates the measured sticking probabilities means a DF using a lower fraction of exact exchange will most likely describe the  $O_2$  + Cu(111) system with high accuracy. Furthermore, our work shows evidence for the presence of both indirect and direct dissociative chemisorption. The indirect precursor-mediated mechanism occurs for low-incidence energy O2. The mechanism is supplanted by a direct dissociative mechanism at higher incidence energies. Lastly, our work suggests that the Cu surface temperature may also effect the dissociation mechanism, but this still needs further verification with a different theoretical framework that allows for the simulation of surface temperature.

# 5.1 Introduction

The adsorption or dissociative chemisorption (DC) of oxygen molecules  $(O_2)$  on metal surfaces is the first step in many oxygen-related chemical processes <sup>6,212,213</sup>. These can be useful processes as seen in, for instance, the heterogeneous catalysis of methanol formation<sup>27,29</sup> or oxidative catalysis reactions<sup>215–218</sup>. But processes can also be undesired, for example in unwanted oxide formation during catalysis or in the corrosion of metal materials<sup>215,216,218,306,307</sup>. As a result, the study of the DC of O<sub>2</sub> on metal surfaces is not only of fundamental but also of high practical importance<sup>1,218</sup>. Furthermore, copper (Cu) is one of the most widely studied transition metals for catalytic activity, both experimentally 68,76,308-<sup>315</sup> and theoretically 55,56,126,129,316-320. In addition, the H<sub>2</sub> on Cu(111) system is well known as a benchmark system for activated DC reactions on transition metal surfaces $^{55,56,110,221,263,321}$ . However, the electronic structure of  $O_2$  + Cu(111) is considerably more complicated than that of  $H_2$  + Cu(111) due to the high electron affinity of the molecule and the triplet-spin ground state of the molecule $^{124,145,228,231,280,319}$ . The O<sub>2</sub> on Cu(111) system has seen plenty of experimental and theoretical development<sup>313,319,322-325</sup> and is as a useful benchmark system for the interaction of O<sub>2</sub> with transition metals.

The majority of studies on  $O_2$  + Cu(111) and other Cu surfaces have focused on the initial sticking probability ( $S_0$ ) of  $O_2$  impinging on the Cu surface<sup>313–315,318,319,324–326</sup>. The studies generally show that the (110) and (100) surfaces have a higher reactivity towards  $O_2$  than the (111) surface, i.e., the sticking probability as a function of the normal component of the incidence energy of the  $O_2$  molecule is highest for the more "open" (110) and (100) faces<sup>314,315,324–326</sup>. The literature generally describes two possible mechanisms for the sticking of  $O_2$  on Cu surfaces, where the sticking of the molecule to the metal surface can proceed via a direct DC reaction or via a non-dissociative chemisorbed (or even physisorbed) precursor state.

The first of these two mechanisms is discussed in the work of Hall et~al. for  $O_2$  on  $Cu(100)^{326}$  and of Zhang et~al. for  $O_2 + Cu(111)^{325}$ . Both provide evidence that  $O_2$  sticking on Cu(100) and Cu(111) takes place largely through direct activated  $DC^{325,326}$ . Additionally, the  $S_0$  on both surfaces appear to follow normal energy scaling (NES), i.e., the  $S_0$  only depends on the normal component of the

incidence energy of the molecule ( $E_i^{-1}$ ). Both works<sup>325,326</sup> also found that the  $S_0$  is positively and linearly correlated with the Cu surface temperature ( $T_s$ ). Interestingly, the work of Zhang  $et\ al.$ <sup>325</sup> seems to indicate a deviation from this linearity of  $O_2$  sticking on Cu(111) at the lowest  $T_s$  shown (90 K), however, the exact  $T_s$  at which such a deviation of linearity starts to occur is not clearly determined<sup>325</sup>. Hall  $et\ al.$  also showed evidence for a considerable energy transfer from the incidence energy ( $E_i$ ) of the impinging  $O_2$  to the Cu(100) surface atoms<sup>326</sup>. It is plausible that such energy transfer also occurs for  $O_2$  sticking on Cu(111), but the work of Zhang  $et\ al.$  did not specify this.

Importantly, the work of Zhang  $et\ al.^{325}$  seems to be in stark disagreement with the  $O_2$  on Cu(111) sticking measurements of Minniti  $et\ al.^{324}$  which predate the work of Zhang  $et\ al.^{325}$  by about ten years. Although the work of Minniti  $et\ al.$  was focused on the sticking of  $O_2$  and  $H_2$  on Cu monolayers on a Ru(0001) surface, they also reported  $O_2$  sticking probabilities for a clean Cu(111) surface. The  $S_0$  measured by Zhang  $et\ al.^{325}$  are considerably higher than those of Minniti  $et\ al.^{324}$ . The authors of Ref.  $^{325}$  also noted this discrepancy but were unable to explain the major disagreements between measurements, even though both experiments were similar in conditions and both used the King and Wells (K&W) technique  $^{69}$ . This does raise the question of what the actual reactivity of  $O_2$  on Cu(111) is.

The second, indirect, mechanism for the sticking of  $O_2$  is supported by the experimental and theoretical works of Refs.  $^{313-315,318,319,322,323}$ . This second mechanism, which proceeds via a precursor state, usually occurs at low  $E_i$ . Already in 1979, Habraken *et al.* published work<sup>313</sup> studying the  $O_2$  chemisorption on Cu(111) using low energy electron diffraction (LEED) and ellipsometry. Based on the dependence of the  $S_0$  on both  $T_5$  and the  $O_2$  surface coverage they argued that  $O_2$  would have to dissociate on Cu(111) via a "mobile" precursor state. Additionally, in 1993 Hodgson *et al.* extensively discussed sticking results for  $O_2$  on  $Cu(110)^{315}$  obtained with the K&W technique<sup>69</sup> and distinctively identified two separate DC channels. The first channel, which occurs for low  $E_i$ , seems to be a precursor-mediated dissociation, and the second at higher  $E_i$  was identified as direct DC. A similar two-channel observation was made in 2004 for the sticking of  $O_2$  on Cu(100) by Junell *et al.*<sup>314</sup>. Furthermore,

in 1996 Sueyoshi *et al.* identified the existence of an adsorbed molecular  $O_2$  species on a 100 K Cu(111) surface<sup>322</sup> using high-resolution electron energy loss spectroscopy (HREELS). This chemisorbed  $O_2$  species dissociated upon annealing the Cu surface to 170 - 300  $K^{322}$ .

The second mechanism, and the presence of at least two reaction channels for O<sub>2</sub> on low index faces of Cu, is similarly supported in theoretical work <sup>318,319,323</sup>. In support of the work of Sueyoshi et al.<sup>322</sup>, Xu et al.<sup>323</sup> used density functional theory (DFT)<sup>121,122</sup> calculations at the generalised gradient approximation (GGA) level with the PW91<sup>188</sup> density functional (DF) to calculate the binding energies of molecularly chemisorbed O<sub>2</sub> on Cu(111). They found energy barriers to dissociation from this precursor state of about 16 - 22 kJ/mol, depending on whether or not the Cu(111) surface is allowed to relax in response to the presence of the adsorbed O<sub>2</sub><sup>323</sup>. Also using the PW91 DF, Martin-Gondre et al. constructed a complete six-dimensional (6D) static surface potential energy surface (PES) for O<sub>2</sub> + Cu(100), using the FPLEPS model<sup>210,247,248</sup> to fit the DFT data, and simulated the DC with quasi-classical trajectory (QCT) calculations<sup>318</sup>. The computed reaction probabilities considerably overestimated the existing experimental results. The authors also identified two distinct reaction channels (direct and indirect), with the fractional contribution of the indirect channel being greatest at low  $E_i^{\perp}$  and declining as  $E_i^{\perp}$  increases<sup>318</sup>.

Lastly, in an attempt to reproduce the experimental work of Minniti *et al.*<sup>324</sup> Ramos *et al.*<sup>319</sup> used the more repulsive, i.e., less reactive, RPBE<sup>239</sup> GGA DF to compute the sticking probabilities of  $O_2$  on Cu(111) (and also  $O_2$  on  $Cu_{ML}$ /Ru(0001)) with the QCT method. They used the corrugation reducing procedure (CRP)<sup>201,202</sup> to fit the DFT data and the Cu surface atom motion was modelled using the generalised Langevin oscillator (GLO)<sup>327</sup> method. Their computed  $S_0$ <sup>319</sup> overestimated the experimental  $S_0$  of both Ref. <sup>324</sup> and Ref. <sup>325</sup>. However, Ramos *et al.* likewise identified the existence of a precursor-mediated dissociation channel in  $O_2$  + Cu(111). Moreover, they found that at  $T_S$  = 100 K the greater part of the  $S_0$  is caused by the non-dissociative chemisorption of  $O_2$  molecules on the Cu(111) surface, in contrast to  $T_S$  = 350 K, where nearly all chemisorption was dissociative<sup>319</sup>.

To properly understand the two reaction mechanisms or channels and distinguish between them, it will probably be necessary to compute the reaction probabilities within chemical accuracy, i.e. within an accuracy of  $1 \text{ kcal/mol}^{55,56}$ . However, the substantial overestimation of the measured  $S_0$  for  $O_2$  on Cu(111) with even the least reactive GGA DF<sup>319</sup>, i.e., RPBE, is concerning, as this suggests that a chemically accurate description of the reaction is likely not possible at the semi-local (GGA) DFT level<sup>319</sup>. This problem is not unique to the dissociation of  $O_2$  on Cu surfaces but is also a well-documented issue for the activated direct dissociative chemisorption of  $O_2$  on Al(111) considered in an electronically adiabatic framework<sup>124,228–230,234–238,240</sup>. Moreover, the failure of semi-local GGA DFT is likely caused by the same origin<sup>124</sup>, and may also be resolved by the same solution as tried recently for  $O_2$  + Al(111)<sup>124,226,280</sup>.

The failure of semi-local (GGA or meta-GGA) DFs to accurately describe the reaction of  $O_2$  on Al(111) has been attributed to the charge transfer energy ( $E_{CT}$ ) of the system being below  $7 eV^{124}$ . Here  $E_{CT}$  is defined as the work function of the metal surface minus the electron affinity of the molecule.  $E_{CT}$  is a measure to investigate the likelihood of electron transfer from the metal surface to the molecule during their collision 124. It is not yet fully understood why  $E_{CT} < 7 \text{ eV}$ results in a failure of semi-local DFs for DC on metals. As discussed in Ref. 124, for gas-phase reactions it has been argued that semi-local exchange-correlation (XC) DFs generally favour, i.e., yield a lower energy for, situations where charge delocalisation occurs<sup>146,328</sup>. This would then result in transition state energies being too low relative to the energies of the reactants and would explain why semi-local DFs applied to Hartree-Fock densities tend to give much better results for gas-phase reactions<sup>147–149,253</sup>. Consequently, such errors have been labelled as "density-driven"<sup>147–149,253</sup>, i.e., as resulting from errors in semi-local densities. However, this explanation is at odds with calculations on O<sub>2</sub> + Al(111), which showed that quite reasonable results can be obtained for this system using semilocal densities provided that a screened hybrid functional was applied to these densities in a non-self-consistent way  $^{124,145,280}$ . The error made for  $O_2$  + Al(111) should then be labelled as "functional-driven" 124,145,147,253,280. Interestingly, the explanation that the underestimation of gas-phase reaction barriers by semilocal density functionals should be due to density-driven errors is now under scrutiny: recent papers argue that the improved agreement resulting from the

non-self-consistent application of semi-local density functionals to Hartree-Fock densities is due to cancellation between functional-driven and density-driven errors<sup>150,151</sup>.

The  $E_{CT}$  of  $O_2$  + Cu(111) is approximately  $4.4 \ eV^{124}$ , thus also substantially below the  $7 \ eV$  boundary. This could be a good reason why one of the least reactive GGA DFs (RPBE) is still too reactive to describe the  $O_2$  + Cu(111) reaction<sup>319</sup>. As such, the employment of a non-local XC in the form of a screened hybrid DF may, similarly to  $O_2$  + Al(111)<sup>124</sup>, help to resolve the overestimation of the reactivity.

The goal of the present chapter is to investigate whether the use of a screened hybrid DF may result in a better description of the experimentally determined reactivity of  $O_2$  on Cu(111). We do this by constructing a static surface PES using the screened HSE06-1/2x-VdW-DF2 DF, applied self-consistently, and by comparing the resulting sticking probabilities, as computed with QCT, to experiments and other theoretical work. We will show that we were able to, for the first time, compute reaction probabilities that underestimate instead of overestimate the experimental sticking probabilities of  $O_2$  on Cu(111). This indicates that a non-local DF that can describe the measured sticking probability with high accuracy must be within reach. Furthermore, we show that for a static surface there seems to be a significant contribution of the indirect reaction channel to the DC for lower incidence energies of  $O_2$ , and that the indirect reaction does not follow normal energy scaling in contrast to the direct reaction.

This chapter proceeds as follows: Section 5.2.1 will briefly discuss the Born-Oppenheimer static surface (BOSS) approximation, Section 5.2.2 will broadly discuss the choice of screened hybrid DF, and 5.2.3 will discuss the computational setup for the DFT calculations. Then, Section 5.2.4 will discuss the CRP PES fitting method, and the details concerning the QCT calculations are found in Section 5.2.5. Thereafter, Section 5.3.1 will discuss the resulting screened hybrid PES, 5.3.2 will compare our computed  $S_0$  with experimental and other computed  $S_0$ , Section 5.3.3 will discuss the direct and indirect components of  $S_0$  and investigate the NES of both components and, lastly, Section 5.3.4 will discuss our results within the framework of current literature. Section 5.4 presents conclusions and an outlook.

# 5.2 Methods

# 5.2.1 The dynamical model

The dynamics calculations are done with the motion of the nuclei decoupled from the motion of the electrons via the Born-Oppenheimer approximation. The Cu atoms are also kept static in their relaxed, or ideal (i.e.,  $0 ext{ K}$ ) lattice position. This results in a total of six degrees of freedom for the motion of the O-atoms (**Figure 5.1A**). The centre of mass (COM) of the diatomic molecule is described by its Cartesian coordinates. Here, Z indicates the distance between the surface and the COM of  $O_2$ , and X and Y describe the projection of the COM on the Cu(111) surface. X and Y are represented in U, V-space such that the angle between the two axes is taken as  $60^\circ$  (see **Figure 5.1B**) to describe the (111) surface unit cell. Furthermore, r is the bond length of the molecule,  $\theta$  the polar angle the  $O_2$  bond makes with the Z-axis, and  $\varphi$  the azimuthal orientation angle of the molecular relative to the Cu surface, as indicated in **Figure 5.1A**. **Figure 5.1B** additionally shows the locations of the high symmetry sites of Cu(111).

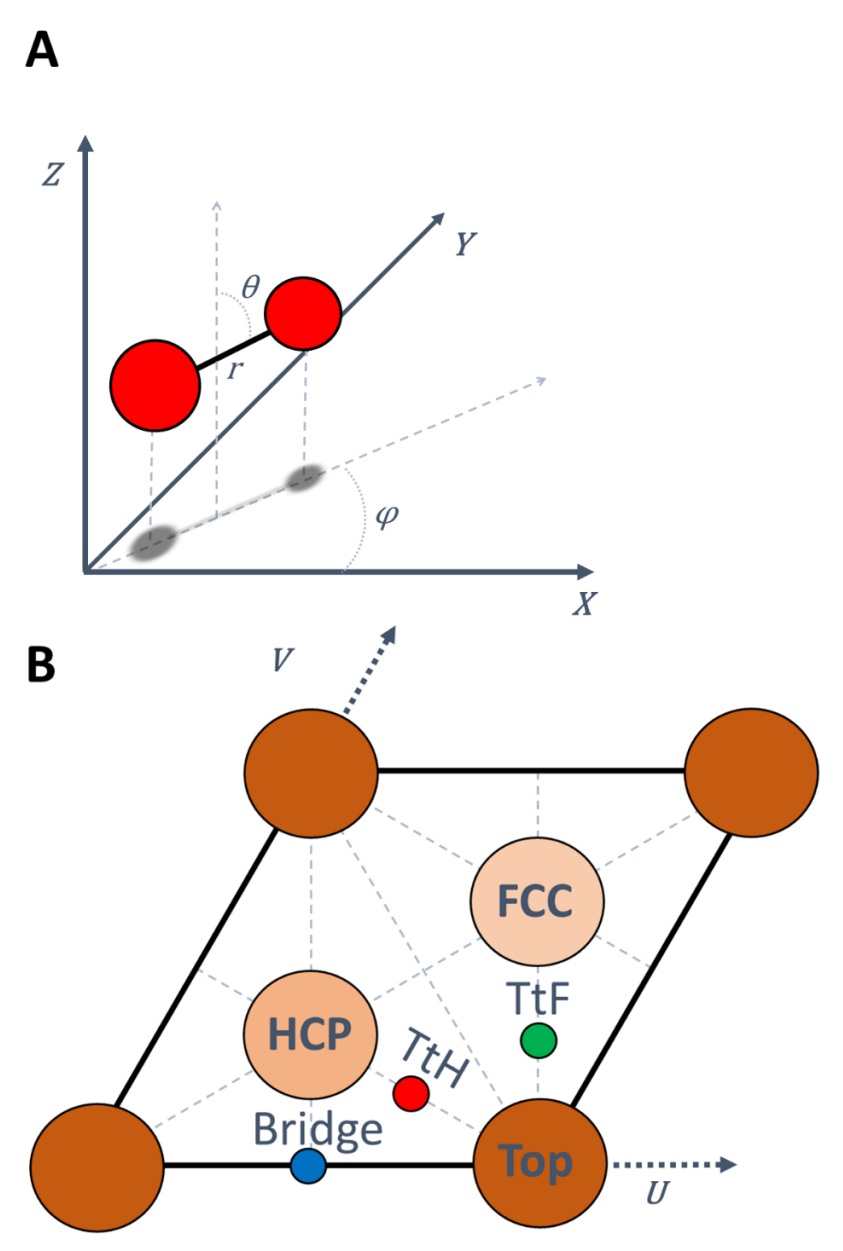


**Figure 5.1**: Coordinate system and its relation to the Cu(111) unit cell; **A**: six-dimensional centre-of-mass coordinate system for the  $O_2$  molecule; **B**: (111) surface unit cell for an FCC metal (like Cu) with all high symmetry sites indicated. A lighter shade represents an atom that is in a deeper layer in the slab.

# 5.2.2 Electronic structure approach

The exchange-correlation functional chosen for this work consists of a combination of two distinct DFs. The first part is the exchange part of the screened hybrid DF named  $HSE06^{189,190}$  but using a fraction of 1/2 of screened exact exchange instead of 1/4. The second part is the Van der Waals DF2 correlation function<sup>195</sup>. Below we will discuss both components and their combination.

The HSE06 DF, based on the better known PBE0<sup>152,153</sup> DF, is a hybrid DF, meaning that a certain fraction ( $\alpha$ ) of exact (i.e., Hartree Fock) exchange( $E^{HF}$ ) is mixed into the PBE<sup>154</sup> exchange-correlation energy ( $E_{XC}$ ) such that

$$E_{XC} = E_C^{PBE} + \alpha E_Y^{HF} + (1 - \alpha) E_Y^{PBE}$$
 (5.1),

here the two  $E_x$  contributions taken together form the exchange part of the exchange-correlation functional and  $E_c$  is the correlation part. HSE06 is distinct from PBE0<sup>152,153</sup> as described by Equation 5.1, due to the addition of screening. Such screening is required for a more physically correct, and more computationally efficient, description of the metal slab<sup>155–157,189</sup>. For example, without screening, the electronic density of states would be substantially and artificially reduced at the Fermi-level<sup>158</sup>.

The screening of the exact exchange is done by introducing a continuous switching function (based on the screening parameter  $\omega$ ) in the coulomb operator describing the electron-electron interaction<sup>189,190</sup>, such that the long-range electron-electron interaction is only described with the semi-local exchange DF<sup>189,190</sup>. This results in the following description:

$$E_{XC}^{HSE06}$$

$$= E_c^{PBE} + \alpha E_x^{HF,SR}(\omega) + (1 - \alpha) E_x^{PBE,SR}(\omega) + E_x^{PBE,LR}(\omega)$$
(5.2),

where SR indicates a short-range interaction relative to the screening parameter  $\omega$  and LR a long-range interaction.

In this work, we opted to use  $\alpha = 1/2$ , calling the corresponding exchange DF HSE06-1/2x. The original HSE06 DF comes with an  $\alpha$  of  $1/4^{152,153,189,190}$ . However, previous work on the interaction of  $O_2$  + Al(111) showed that even  $\alpha = 1/3$  resulted in reaction probabilities that overestimated the experimental results  $^{124,280}$ . Therefore, we opted to increase the  $\alpha$  to 1/2 (in principle the

maximum mixing value<sup>152</sup>), assuming that a higher fraction of exact exchange should also be required to reproduce the barrier height for  $O_2 + Cu(111)^{283}$ . This value may seem high but we note that the BH&HLYP and MPW1K functionals, with values of  $\alpha$  of 0.5 and 0.428, respectively, were found to perform quite well on gas-phase barriers in the work of Truhlar and co-workers<sup>329</sup>. Moreover, keeping in mind the addition of the Van der Waals correlation in the DF, as described below, we anticipated that we might require a high fraction of exact exchange to compensate for the expected effect<sup>56,124,126,132,282</sup> this correlation might have on the barrier heights, and thus on the computed reaction probabilities.

In the HSE06-1/2x DF, the correlation functional is the PBE correlation functional. However, semi-local DFs like PBE are not able to describe long-range interactions between electrons and the non-local or global nature of the (screened) hybrid DF does not include a correct description of the attractive Van der Waals correlation. Therefore we opted to use a non-empirical Van der Waals (VdW) DF as correlation DF<sup>183,195</sup> to improve the long-range correlation description of the functional. To obtain the so-called PBE-VdWDF2 DF, which we use as a 'primer' (see Section 5.2.3), the addition of Van der Waals correlation is rather straightforward:

$$E_{XC} = E_C^{LDA} + E_C^{VdWDF2} + E_X^{PBE}$$
 (5.3).

Here the correlation part of the DF is now split between that of the local density approximation (LDA) and a purely non-local VdW correlation correction <sup>195</sup>. This correction is computed with

$$E_c^{VdWDF2} = \int d\mathbf{r} \int d\mathbf{r}' \, \rho(\mathbf{r}) \Phi(\mathbf{r}, \mathbf{r}') \rho(\mathbf{r}')$$
(5.4),

in which r and r' are the position vectors of the electron density,  $\rho(r)$  the electron density of the electron at r, and  $\Phi(r,r')$  is the Van der Waals kernel describing the electron density-density interaction. The details of this kernel are complex and out of scope for this chapter and we refer the interested reader to Refs.  $^{183,195}$  for more information.

The addition of the VdW correlation is expected to introduce a VdW well in front of the barrier in the entrance channel<sup>56,126,130,282</sup>. A VdW-well would speed up the molecule as it approaches the Cu(111) surface (during dynamics calculations) and this could influence the dynamics of the reaction<sup>126,130</sup>. The replacement of

PBE correlation with VdW-DF2 correlation may lower the reaction barrier. Anticipating that this may lead to a too-low barrier we decided to use a high fraction of exact exchange, as discussed above. However, it must be noted that a lowering of the barrier does not always occur and replacing PBE with VdW-correlation has in the past sometimes caused the opposite to happen<sup>132</sup>. As the results will show, choosing the maximum fraction of exact exchange,  $\alpha$ , to "tune" a barrier height is still a trial-and-error-based approach.

In conjunction, the combination of exact exchange and VdW-correlation leads to the following expression for the screened hybrid VdW exchange-correlation energy of the HSE06-1/2x-VdWDF2 DF:

$$E_{XC}^{HSE06-1/2x-VdWDF2} = E_{C}^{LDA} + E_{C}^{VdWDF2} + \frac{1}{2}E_{x}^{HF,SR}(\omega) + \frac{1}{2}E_{x}^{PBE,SR}(\omega) + E_{x}^{PBE,LR}(\omega)$$
(5.5).

It is important to distinguish this DF from other screened hybrid VdW DFs, as a simple combination of two established DFs, as described above. Our functional does not represent a completely new screened hybrid VdW DF, like the recent VdW-DF2-ahbr DF as developed by Hyldgaard and co-workers in such a way that the exchange part of the functional is matched to the Van der Waals part<sup>193</sup>. It was expected that the HSE06-1/2x-VdWDF2 DF would adequately describe longer-range interactions and thereby result in the presence of a VdW-well before the barrier<sup>126124</sup>, and we hoped that it would correctly describe the barrier height<sup>124</sup>.

# 5.2.3 Computational details of the DFT calculations

The DFT calculations are done with the Vienna Ab Innitio Simulation Package (VASP) version 6.3.2<sup>200,258–262</sup>, with the Van der Waals implementation of J. Klimeš *et al.*<sup>285,286</sup>. All computed DFT energies are based on two different successive self-consistent field (SCF) spin-polarised single-point calculations. The first is a "primer" calculation done with the PBE-VdWDF2 DF to establish a decent estimate for the electron densities and Kohn-Sham (KS) wavefunctions. After this, the HSE06-1/2x-VdWDF2 SCF single-point calculation is started using the previously converged PBE-VdWDF2 KS wavefunction. This is done to

meaningfully improve the convergence speed of the calculation with the screened hybrid DF.

Both calculations use a 2x2 4-layer Cu(111) slab with 15 Å of vacuum separating the slabs. The lattice constant for Cu was converged with the HSE06-1/2x-VdWDF2 DF to 3.698 Å, and relative to the bulk the top interlayer distance was reduced by 1.0%. This interlayer relaxation is chosen based on experimental work, which indicates that at the interface with the vacuum changes in the interlayer spacings of Cu(111) are only significant between layers one and two, the relevant change being about 1.0% for low-temperature Cu(111)<sup>330</sup>. Moreover, experimental Cu lattice interlayer distances have been used successfully in theoretical work in the past<sup>321</sup>. An energy cutoff of 440 eV and an 8x8x1 Γ-centred k-point grid is used. The core electrons are represented with the augmented wave (PAW) method<sup>199</sup>. Specifically, the GW projector pseudopotentials developed for PBE as implemented in VASP were used. The GW versions were used to both improve convergence and improve upon the lattice description of Cu using the HSE06-1/2x-VdWDF2 DF. To ease convergence even more, Methfessel-Paxton smearing with a width of 0.2 eV is used.

The primer (PBE-VdWDF2) single point energy was converged using the conjugate algorithm implemented in VASP, using a very tight convergence criterion, i.e.,  $10^{-9}$  eV. This is done to best approach the variational minimum of the electronic density, thus possibly making it a better KS wavefunction starting point for the screened hybrid single point, in line with earlier published work for  $O_2$  on Al(111)<sup>280</sup>, i.e., Chapters 3 and 4. Finally, the HSE06-1/2x-VdWDF2 single-point energy is converged self-consistently using the damped algorithm to within  $10^{-5}$  eV, using a sparser (or as indicated in VASP; fast) FFT-grid (fast Fourier transform-grid) for the exact exchange (HF) calculations. The faster grid was chosen as the computational cost with the normal FFT grid would not be manageable, i.e., we would not get the calculations converged. Based on a section of PES data points for  $O_2$  + Al(111) presented in Chapter 4, i.e., 4035 out of the complete 5250, we estimated that the root mean squared error(RMSE) introduced in the PES by using the sparser HF-FFT-Grid is about 0.9 kJ/mol. We assume that the error for  $O_2$  + Cu(111) will be of a similar magnitude, therefore,

this should not be detrimental to the accuracy of results published in this chapter.

# 5.2.4 Fitting the PES

The  $O_2 + Cu(111)$  6D interaction is described by a continuous spline interpolation of 5260 computed DFT single points. These 5260 points make up a grid describing the  $O_2$  + Cu(111) interaction and a grid describing the molecule in the gas-phase above the surface. The interaction grid spans 29 combinations of Cu surface sites and  $O_2$  orientations, i.e., 29 different sets of U, V,  $\theta$  and  $\varphi$ coordinates (see Figure 5.1) as also used in previous chapters and other, similar, work<sup>124,130,280</sup>. For each combination of surface site and molecular orientation, the same r and Z grid is set up (see Figure 5.1); where r = [1.000, 1.100, 1.150,1.175, 1.190, 1.200, 1.225, 1.250, 1.300, 1.400, 1.500, 1.600]  $\mathring{A}$  and Z = [1.00, 1.00]1.50, 2.00, 2.25, 2.50, 2.75, 3.00, 3.25, 3.50, 3.75, 4.00, 4.25, 4.50, 4.75, 5.00] Å. The computational time involved in converging the calculations of the 5260 DFT single points with the HSE06-1/2x-VdWDF2 DF was more than 25 million CPU hours (300 – 330 elapsed hours per single point using dual-processor nodes, i.e., using nodes containing two octo core 2.4GHz EM64T Xeon E5 processors (E5-2630 v3), or two octo core 2.6GHz EM64T Xeon E5 processors (E5-2650 v2)), thus starting to push the limits of computational feasibility.

The continuous PES spline-interpolation fitting quality was improved by employing the corrugation-reducing procedure (CRP) $^{201,202}$  as also done in previous chapters and Refs.  $^{124,263,280}$  Herein, two atom-surface, 3D, PESs of O interacting with the Cu(111) surface, are subtracted from the molecular, 6D, PES to obtain a 6D function with less corrugation. This function therefore easier to fit accurately. After fitting, the atomic PES is re-added to the fitted result. The procedure is implemented for this chapter along similar lines as in Refs.  $^{124,280}$ . Previously, the application of the CRP resulted in a fitting RMSE of  $0.8 \, kJ/mol$  as long as the interaction energies were smaller than  $4 \, eV^{126}$ , where outliers often remain below  $2.9 \, kJ/mol^{115,202}$ . This error is generally small enough to ensure that using the CRP-PES tests the quality of the underlying DFT data.

The atomic 3D PES as needed for the CRP does not necessarily need to be very accurate as it (and its possible inaccuracies) are first subtracted and later readded to the molecular PES. However, for the procedure to work it does need to be physically reasonable<sup>124</sup>, based on a dense Z-grid, and free of unwanted fluctuations, inconsistencies, and discontinuities. Achieving these standards with spin-polarised calculations and a computationally demanding DF is difficult for an open shell system like atomic O + Cu(111). To resolve this we make use of the flexibility in the accuracy, i.e., we opted to use spin unpolarised DFT calculations using the PBE-VdWDF2 DF and to impose a fairly tight convergence criteria of  $5.0 \cdot 10^{-7}$  eV to calculate the O + Cu(111) 3D PES. All other computational details were kept consistent with the previously discussed "primer" single-point calculations. A CRP 6D PES computed with a similar procedure has been successfully developed and tested for  $O_2 + Al(111)^{124,280}$ . Additionally, we believe that the PBE-VdWDF2 DF will capture the longer range O + Cu(111) interaction well enough not to disrupt the CRP interpolation and that it will allow us to achieve the high precision standard needed without excessively consuming computational resources.

# 5.2.5 Quasi-classical trajectory dynamics calculations

With the continuous 6D PES it is possible to run dynamics calculations of  $O_2$  impinging on the Cu(111) surface. Here the dynamics calculations are performed with the quasi-classical trajectory (QCT)<sup>210,211</sup> method. In QCT the  $O_2$  molecule is given an initial zero-point energy after which its reaction with the Cu surface is propagated classically through time<sup>210,211</sup>. More extensive details on our implementation of the QCT method can be found in Refs. <sup>130,136</sup>. Here, the  $O_2$  molecule is given an initial rovibrational energy (or assigned to a rovibrational state) at  $7.0\,\text{Å}$  above the Cu(111) surface with a given incidence energy, along an incidence vector pointing towards the surface at an angle  $\Theta$  with the surface normal.

The outcome of a trajectory is determined by the molecule encountering specific conditions that also lead to the termination of the trajectory. The first is when the bond length (r) of the  $O_2$  molecule exceeds  $1.59\,\text{Å}$ . At this point, the molecule is considered dissociated and thus the trajectory is counted as reacted. If the

molecule-surface distance exceeds  $7.0\,\text{Å}$  and the molecule moves away from the surface the trajectory is considered scattered. Lastly, if the propagation time limit of  $1\,\text{ns}$  is reached without encountering either state, the molecule is considered trapped on the surface. However, we observed that the majority of  $O_2 + Cu(111)$  interactions lead to scattering or reaction within the first  $10\,\text{ps}$ .

Both in scattering and reaction we make an additional distinction between direct and indirect events. Indirect events occur when the  $O_2$  molecule makes an extra bounce on the surface before reaching terminating conditions. A bounce is defined by a sign change from negative to positive along the *Z*-component of the momentum vector of the COM of the  $O_2$  molecule, i.e., a bounce occurs whenever the molecule changes from going towards the surface to away from the surface. An event is considered indirect if the number of bounces is larger than one. For direct scattering the number of bounces is thus equal to one and for direct dissociative chemisorption the number of bounces can be equal to or smaller than one. We note that with our definition of indirect trajectories, their associated timespan may be too short to directly detect their presence experimentally.

All together, we distinguish between direct scattering, indirect scattering, direct reaction, indirect reaction, and trapping as possible events. The probability of a particular event,  $P_E$ , is easily defined as

$$P_E = \frac{N_E}{N_{Total}} \tag{5.6},$$

where  $N_E$  is the number of trajectories counted as resulting in a particular event and  $N_{Total}$  is the total number of trajectories run. Furthermore, if trapping is a relevant event one needs to define the total sticking probability ( $S_0$ ) as the sum of contributions from dissociative chemisorption and trapping, such that

$$S_0 = 1 - P_s = P_r + P_t (5.7),$$

where  $P_s$  is the scattering probability (direct plus indirect),  $P_t$  is the trapping probability and  $P_r$  is the reaction probability (direct plus indirect).

Experimental sticking probabilities are usually extracted from molecular beam studies. In a molecular beam, the  $O_2$  molecules are not in a single rovibrational state but rather in a distribution of states according to experimental conditions. The rovibrational state distribution of the  $O_2$  molecule follows from the nozzle

The (normal) incidence energy of the molecule is experimentally varied by either changing the seeding ratio of the molecular beam (by mixing the  $O_2$  with lighter or heavier nobles gasses) or by varying the incidence angle  $\Theta$ . With the QCT method, we can look at "monoenergetic" beams, i.e., beams with a constant incidence energy, where we can vary  $\Theta$ . However, if the experimental time of flight (TOF) spectra of the  $O_2$  beams are known we can more closely simulate the experiment by simulating the flux-weighted incidence velocity distribution (N(V)) using

$$N(V)dV = K_V V^3 e^{-\frac{(V - V_S)^2}{(\Delta V_S)^2}} dV$$
 (5.8),

where  $K_V$  is a proportionality constant, V is the velocity of the molecule,  $V_S$  is the stream velocity and  $\Delta V_S$  the width of the velocity distribution<sup>67</sup>. This can be rewritten to an energy distribution by using the kinetic energy velocity relation:

$$E_S = \frac{1}{2} m V_S^2 (5.9),$$

and by defining:

$$\frac{\Delta E_S}{E_S} \equiv \frac{2\Delta V_S}{V_S} \tag{5.10},$$

such that the flux-weighted incidence energy distribution is written as 67

$$N(E)dE = \frac{1}{K_E} E e^{-4E_S \frac{(\sqrt{E} - \sqrt{E_S})^2}{(\Delta E_S)^2}} dE$$
 (5.11),

where  $K_E$  is a normalisation constant. In practice, this means that, just like the incidence velocity distribution, the distribution of the incidence energy of  $O_2$  is described by a slightly skewed Gaussian. The velocity distribution

characterisations for the experiments of Zhang *et al.*<sup>325</sup>, and our fitted parameters characterising their beams are described in the first appendix, i.e., Section 5.5.1 We refer the reader to the work and electronic supporting information of Zhang *et al.*<sup>325</sup> for more details regarding their molecular beam time-of-flight measurements, velocity distributions, and energy distributions.

#### 5.3 Results and discussion

# 5.3.1 PES analysis

Six different two-dimensional "elbow" cuts through the PES are shown in **Figure 5.2**, to get an impression of the PES. Geometries (U, V,  $\theta$ ,  $\varphi$ , r, Z) and heights of the barriers shown in **Table 5.1** represent the barriers shown with the white dots in **Figure 5.2**.

**Table 5.1**: Barrier in r, Z, and E per elbow cut, as displayed in **Figure 5.2**; if available the barrier height of Ramos et al.<sup>319</sup> is displayed in brackets. Energies in eV, distances in Å, the underlined barrier is the lowest barrier found for all 29 different elbow cuts, see Section 5.2.4.

Geometry	r <sub>barrier</sub> (Å)	Zbarrier (Å)	Ebarrier (Ebarrier Ramos et al. 319) (eV)
Bridge, $\theta$ : 90°, $\varphi$ : 0°	1.22	2.43	<u>0.28</u> (0.097)
Top, θ: 0°	n/a	n/a	n/a
Bridge, $\theta$ : 90°, $\varphi$ : 60°	1.22	2.29	0.35
Top, θ: 90°, φ: 0°	1.26	2.14	0.41
Bridge, $\theta$ : 90°, $\varphi$ : 90°	1.23	2.21	0.39
FCC, θ: 90°, φ: 0°	1.22	2.24	0.32 (0.202)

Following an incoming  $O_2$  molecule, the elbow cuts show a few general trends. First, coming from the gas-phase a small and shallow ( $\approx 2~kcal/mol$ ) well appears between 5 and 3 Å above the surface. The distance of the Van der Waals well to the surface and its depth is, to a large extent, independent of the  $O_2$  (U, V) impact site above the Cu(111) surface (see **Figure 5.2**, and **Figure 5.10** of Section 5.5.2). However, the Van der Waals interaction does depend on the polar angle of orientation of the molecule. The well is shallower and further from the surface if the molecule is not oriented parallel to the surface (see **Figure 5.10**). The dependence noted suggests that trapping of the molecule will occur through a mechanism in which energy in translational motion normal to the surface is temporarily converted to rotational energy. If the molecule is not orientated

along the surface normal, it encounters a barrier to molecular chemisorption at a slight bond elongation and  $Z \approx 2.3 \,\text{Å}$ . The barrier height is dependent on surface site and molecular orientation but its location remains roughly similar. Once this barrier is overcome the molecule enters what looks like a molecular chemisorption-well (except for the upright geometry in Figure 5.2B), where the  $O_2$  bond length is expanded to between 1.3 and 1.5  $\mathring{A}$  at about 2  $\mathring{A}$  above the surface. Some channels (Figure 5.2C and Figure 5.2E) seem to allow for further dissociation (i.e. expansion of the bond length beyond the value of 1.59 Å, where it is considered dissociated in the dynamics) without the need for overcoming an additional barrier that is higher than the entrance-barrier (Figure 5.2C and Figure 5.2E). However, for most other combinations of molecular orientation and surface site the second (exit channel) barrier, if present, would appear to be higher than the first barrier encountered, for example, in Figure 5.2D and Figure 5.2F. This seems to indicate that for molecules with low-incidence energy a pathway to dissociation is possible as long as the molecularly chemisorbed O<sub>2</sub> species (i.e., after crossing the first barrier) can change its geometry  $(U, V, \theta)$ , and  $\varphi$ ) to one in which the second barrier is low enough to allow dissociation. An important assumption made in this chapter is that once the first barrier to molecular chemisorption is crossed and the bond length (r) exceeds 1.59 Å the molecule will find its way over the second barrier to the state where two separate O-atoms remain chemisorbed to the surface (see also below).

The lowest entrance barrier that we found has a height of 0.28 eV (27 kJ/mol) and is located at the bridge site with  $\theta = 90^{\circ}$  and  $\varphi = 0^{\circ}$  (**Figure 5.2A** and **Table 5.1**). However, similar to the findings of Ramos  $et~al.^{319}$  the second, i.e., exit channel, barrier is very high for this geometry, meaning that at low  $E_i$  a change in  $O_2$  adsorption location or orientation is needed to facilitate full dissociation. Unlike the work of Ramos  $et~al.^{319}$ , we seem to find our lowest exit barrier at a different molecular orientation and surface site than the site and orientation of their lowest exit channel barrier. Still, our PES suggests that for low-incidence energies of  $O_2$ , a precursor-mediated pathway to full dissociation is not unexpected.

We note that our PES employs a shorter r-grid(see **Figure 5.2** and Section 5.2.4) than the previous work of Ramos  $et\ al.^{319}$ . The chosen limit of r of  $1.60\ Å$  was

initially based on previous work on  $O_2$  on Al(111). However, for  $O_2$  + Cu(111) the shorter r-grid compared to the work of Ramos et al. 319 means we may artificially underestimate the second, or exit channel, barrier. This artificial underestimation would be the consequence of cutting-off the r-grid before describing the highest point of the barrier, thus lowering the threshold for full dissociation. This may result in increased dissociative reactivity of the PES. However, any increase of the r-grid to improve the second barrier description to the same size as Ramos et al. would come at computational costs that are prohibitive for our present work. For example, if we were to adhere to the current rigorous implementation and methods of the CRP-PES each additional rvalue in the r-grid would come with an additional 435 DFT single-point calculations. This is because the r-grid would need expansion into the full 15point Z-grid and for all 29 combinations of surface site and molecular orientation. Furthermore, at the lowest minimum r-grid accuracy standard of a  $\Delta r$  of 0.1 Å, we would need 9 additional r-values in the r-grid (to expand 1.6 Å to the value of 2.5 Å used in Ref. <sup>319</sup>). Based on the computational costs of this PES (300 - 330 elapsed hours per single point calculation, see Section 5.2.4) we estimate that we would need an additional 18 million CPU hours to facilitate such an r-grid extension.

Lastly, we note that all elbow cuts with parallel orientations (i.e.,  $\theta$ : 90°) through the fitted PES share a small defect in the PES for higher bond lengths further away from the Cu(111) surface. This is due to some DFT calculations in the 3D atomic PES that have not converged as well as others. However, this defect appears in an area where the classical dynamics should hardly ever sample the PES (at  $+1.50\,eV$  in potential energy). Thus, we do not expect to see any influence of this defect on our QCT results.

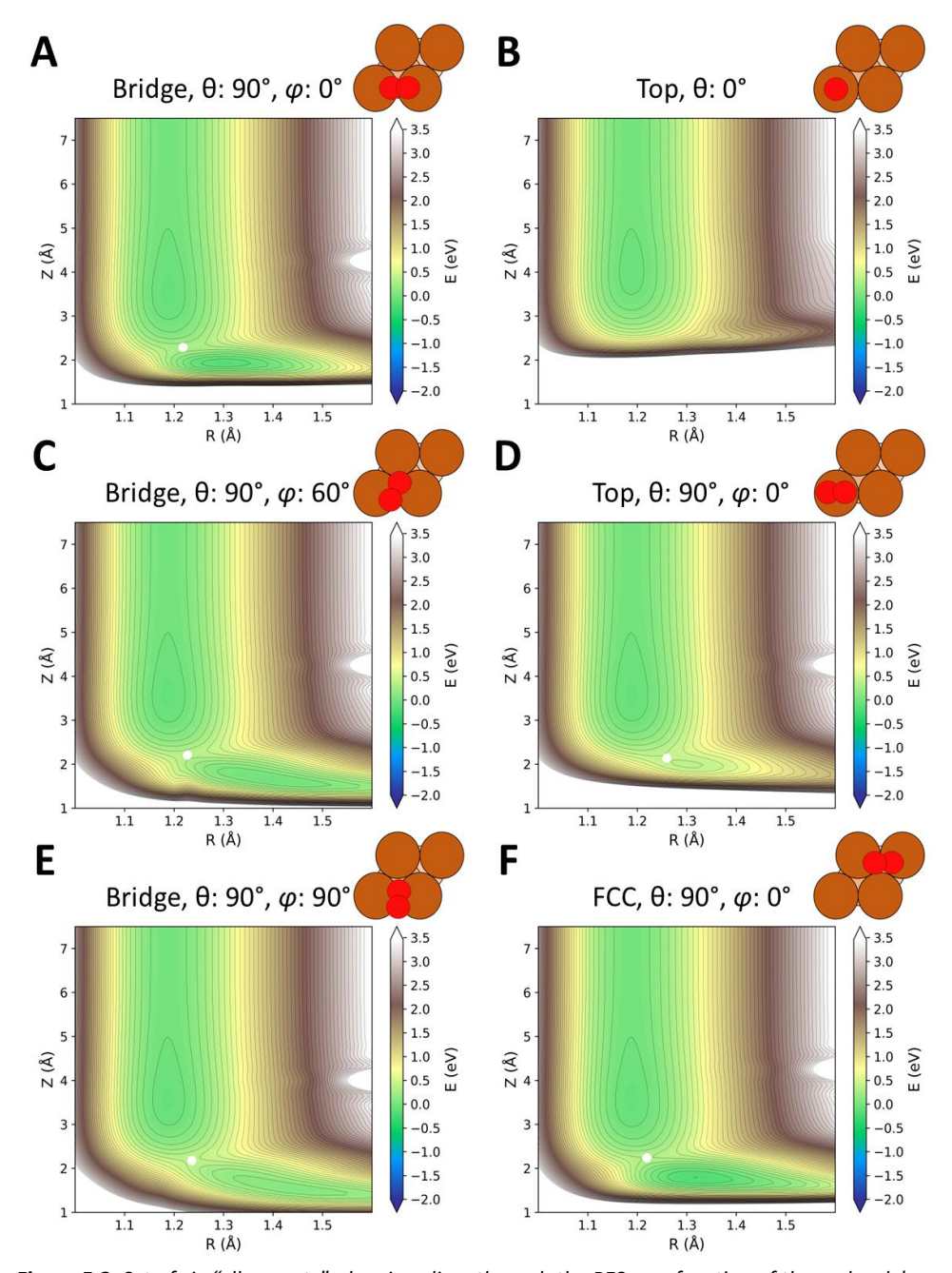


**Figure 5.2**: Set of six "elbow cuts", showing slices through the PES as a function of the molecule's bond length (r) and the distance of  $O_2$  to the surface (Z) for six different geometries (sampling three different surface sites and three different molecular orientations). Contour lines are separated by 2 kcal/mol. The white dots show the location of the barrier(if present) in reduced dimensionality.

## 5.3.2 Dynamics results

The initial conditions of the  $O_2$  beam for the K&W experiments of Zhang et al.<sup>325</sup> are simulated as closely as possible with our QCT calculations. The flux-weighted velocity distributions from the work of Ref. 325 are fitted with Equation 5.8 using a least-squared fitting method, see Section 5.5.1. The fitting of the velocity distribution results in slightly different average incidence translational energies than those presented by Zhang et al. but the difference is within 10 meV. In addition to the  $O_2$  in He seeding ratios, the incidence angle  $\Theta$  was varied to change the  $E_i^{\perp}$  (similar to the work of Zhang et al.). The resulting  $S_0$  (based on 500k trajectories per  $E_i^{\perp}$ ) are presented in **Figure 5.3**. The corresponding error bars are generally smaller than the representation of the datapoint. The figure additionally shows the experimental  $S_0$  of Minniti et al.<sup>324</sup>(blue diamonds) and Zhang et al. 325 (black diamonds), and the semi-local RPBE DF sticking probabilities of Ramos et al.  $^{319}$  (green solid line) for comparison. We also present calculated  $S_0$ for single values of  $E_i^{\perp}$ , where 100k trajectories were run for every 4 meV (0.39) kJ/mol) of normal incidence energy ranging from 12 meV to 2000 meV (see Figure 5.3 and Figure 5.4). In Figure 5.3B and C these results were cut off at 65 kJ/mol for clarity of the plot.

Our "beam simulated" and "mono-energetic"  $S_0$  overlap substantially, where the beam simulated  $S_0$  starts showing reactivity at a lower average  $E_i^\perp$  and increases slightly slower than the mono-energetic  $S_0$  to eventually reach the same plateau at  $S_0 \approx 0.180$ . Especially at low  $E_i^\perp$ , this is not unexpected as the use of the actual velocity distribution will slightly smear out sticking probability results, as can be inferred from Equation 5.11 and the steep increase of the monoenergetic  $S_0$  at low  $E_i^\perp$ .

More importantly, our results underestimate the  $S_0$  compared to all other  $S_0$  presented in **Figure 5.3**. However, the qualitative agreement with the results of Ramos *et al.*<sup>319</sup> is noteworthy. Both theoretical studies indicate a plateau in  $S_0$  after an initial steep rise of the reactivity. Our barriers to sticking are substantially higher than those of Ramos *et al.* (as also seen in **Figure 5.2** and **Table 5.1**) thus considerably reducing the sticking probability. Agreement with the experiment is best with the results of Minniti *et al.*, as their  $S_0$  are lower than those of Zhang *et al.* 

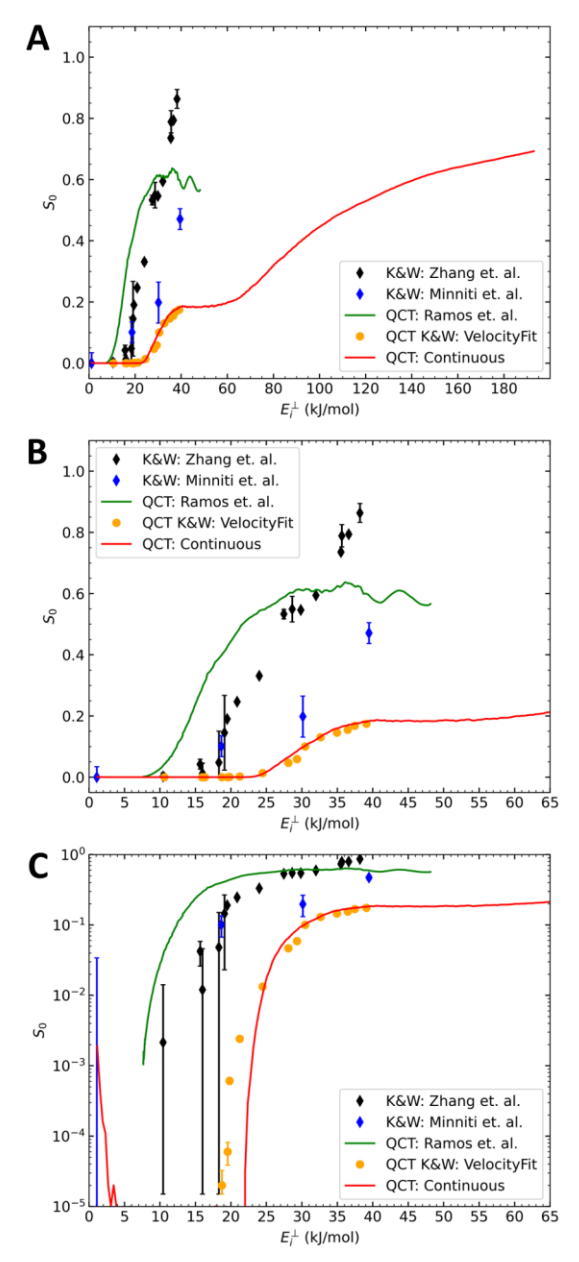


**Figure 5.3**: Sticking probabilities as a function of normal incidence energy; **A**: normal axes; **B**: normal axes, shorter range of the x-axis; **C**: Log y-axis, shorter range of the x-axis. Black diamonds: experimental K&W results taken from Ref.  $^{325}$ ; Blue diamonds: experimental K&W results taken from Ref.  $^{319}$ ; Orange dots: QCT results of present work for the molecular beam with stream velocities based on the fit of the Zhang et al. TOF data using Equation 5.11, 500k trajectories per point; Red line: continuous single  $E_i^\perp$  QCT results of present work based on 100k trajectories per point, one point every 0.39 kJ/mol.

The disagreement with the experiment is more substantial than we would have hoped, however, this is not disheartening. These are, so far as we are aware, the only DFT-based results for the sticking of  $O_2$  + Cu(111) that underestimate experimental results, where thus far, even the least reactive (RPBE) DF would still overestimate the measured sticking probability. This means that the admixing of exact exchange with semi-local exchange in the exchange-correlation DF is a working method to increase the barrier heights for the reaction and to reduce the overall reactivity of the DF. Moreover, as the DF without exact exchange overestimates the sticking probability and the DF with an exact exchange fraction of 1/2 underestimates the reactivity, we may very well be able to find a DF with a lower exact exchange fraction with which we can reproduce the experimental sticking probabilities far more closely.

As already noted in the Introduction, there are fairly large differences between the sticking probabilities measured by Zhang et al. 325 and Minniti et al. 324. These differences occur at high incidence energies but not at low energies, in a region where the sticking probabilities are large (Figure 5.3A and 3B). The observed differences seem consistent with a difference between the cleanliness and the histories of the crystals used in the different experiments as speculated by Zhang et al. 325, and not with the influence of defects like steps that could occur at low surface concentrations. Specifically, one might speculate that with the exposure times in the experiments of Minniti et al. at high incidence energies sticking could occur with averaging over non-zero oxygen pre-coverages, leading to lower sticking probabilities. However, this is mere speculation, and, even worse, speculation by theorists on the origin of experimental differences. At the time of publication of the paper on which this chapter is based, we noted: "Nonetheless, it would be good if additional molecular beam experiments were done on the benchmark  $O_2$  + Cu(111) systems that would conclusively establish both the reactivity of Cu(111) towards  $O_2$  and the origin of the differences between the current experiments." Additionally, calculations could be done looking at the effect of oxygen pre-coverage on sticking, to predict under which regime of oxygen pre-coverages (and therefore molecular beam exposure times) measured sticking probabilities could be significantly smaller than at zero precoverage conditions.

Meanwhile, after the publication of the paper on which this chapter is based, new sticking experiments by Wu  $et~al.^{331}$  have shown good agreement with the sticking probabilities of Zhang  $et~al.^{325}$ . The validation of the results of Zhang et~al. implies that their sticking results can be considered the benchmark for  $O_2$  on Cu(111) over the work of Minniti  $et~al.^{324}$ . Nevertheless, the work presented in this chapter still underestimates all experiments, and therefore the discussions and conclusions of this chapter remain consistent with the original paper that this chapter is based on.

# 5.3.3 Direct or indirect dissociation and normal energy scaling in the QCT dynamics

We have also looked into the two possible reaction mechanisms of  $O_2$  dissociating on Cu(111) that have been discussed in the literature. To do so we have disentangled the mono-energetic  $S_0(E_i^\perp)$  in contributions due to specific events (as discussed in Section 5.2.5) and presented those in **Figure 5.4**.

As discussed before,  $S_0$  can be separated into components  $P_E$  due to several different events. The first is the probability of physisorption or non-dissociative chemisorption in the form of molecular trapping  $(P_t)$ , which may be considered a non-reactive form of sticking. The other part of the sticking probability is dissociative  $(P_r^T)$  and can again be separated into a direct  $(P_r^D)$  and an indirect  $(P_r^T)$  component. All definitions and conditions for these states are discussed in detail in Section 5.2.5. **Figure 5.4** presents mono-energetic probabilities of each of these events for  $E_r^T$  ranging from 12 meV to 2000 meV, for every 4 meV, where 100k trajectories were run per  $E_r^T$ .

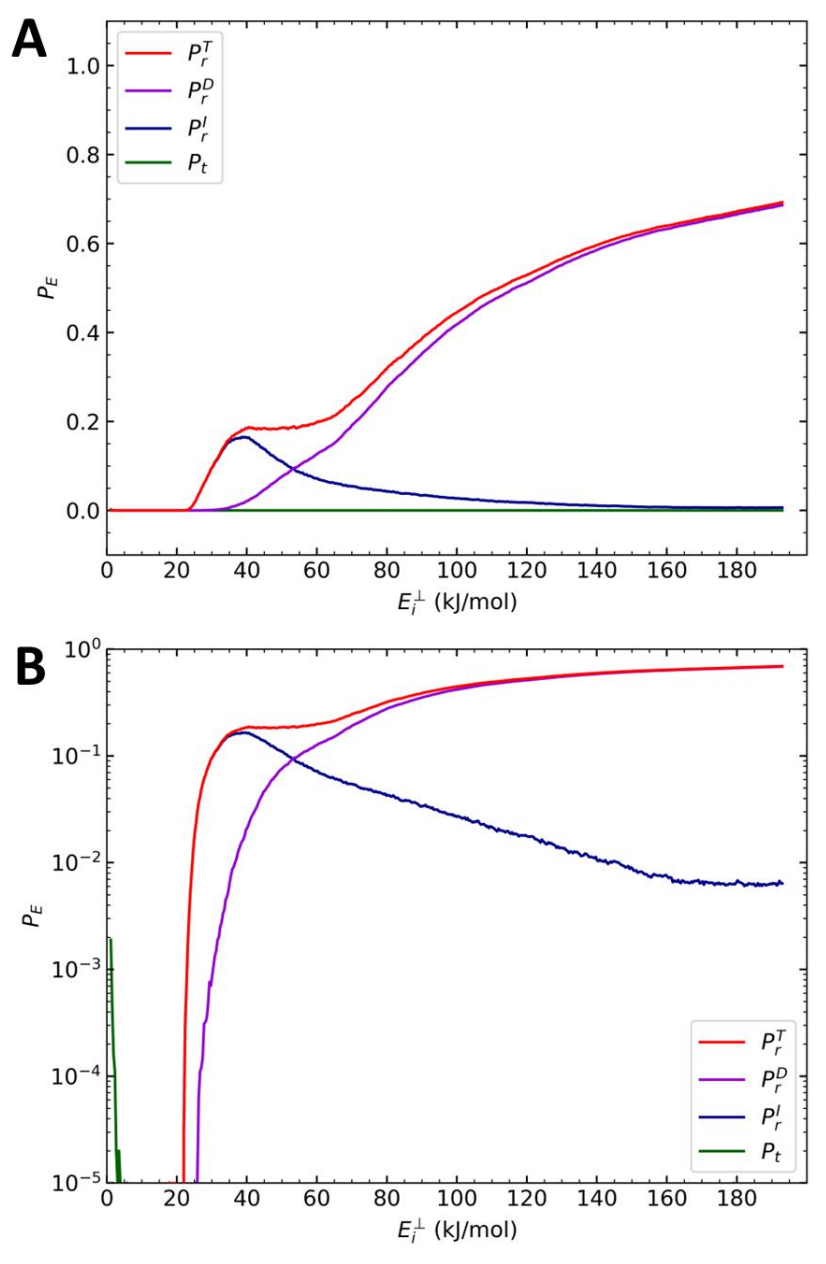


**Figure 5.4**: Decoupled event probabilities as a function of normal incidence energy;  $P_r^T$  is the total reaction probability;  $P_r^D$  is the direct reaction probability;  $P_r^D$  is the indirect reaction probability;  $P_t$  is the trapping probability;  $P_t$ : Event probability;  $P_t$ : log plot of event probability; propagation time of 1 ns per trajectory, 100k trajectories per point, point per  $E_r^D$ : 0.004 eV (0.38 kJ/mol).

**Figure 5.4** shows that, similarly to the findings of Martin-Gondre *et al.* (on Cu(100))<sup>318</sup>, there is both indirect and direct DC. The indirect reaction takes off from  $E_i^{\perp} = 22.0 \, kJ/mol$  and increases in importance up to about  $E_i^{\perp} = 39.5 \, kJ/mol$ . After this, an increase in the  $E_i^{\perp}$  leads to a decreased probability of the indirect reaction, which is reduced to~ $6\cdot10^{-3}$  at  $E_i^{\perp} = 180 \, kJ/mol$ . The direct dissociation reaction takes off at  $E_i^{\perp} = 26.0 \, kJ/mol$  and its probability slowly increases until a kink occurs at  $E_i^{\perp} = 65.0 \, kJ/mol$ , beyond which the reaction probability increases more rapidly to eventually smoothly approach an asymptotic reaction probability of about 0.7 for very high  $E_i^{\perp}$ .

The interplay of these two mechanisms means that the indirect mechanism is dominant for  $E_i^{\perp} \leq 53 \text{ kJ/mol}$  after which the direct mechanism takes over. Furthermore, this change of mechanism causes a plateau to form in the total reaction probability because the decrease of the indirect dissociation is matched roughly by the increase of the direct dissociation. As a result, the total reaction probability remained roughly constant in the range of  $E_i^{\perp} = 45 - 65 \text{ kJ/mol}$ . Furthermore, it is tempting to speculate that the dominance of the direct mechanism seen in **Figure 5.4A** (for  $E_i^{\perp} > 53 \text{ kJ/mol}$ ) could somehow be related to the observation of Cu<sub>2</sub>O formation observed in recent molecular beam experiments of Taleb et al. for incidence energies greater than 0.48 eV332(46 kJ/mol). This formation might result as a consequence of the fast dissociation of oxygen atoms resulting from direct dissociation with subsequent ballistic motion, from clean patches of Cu(111) to patches where the bulk oxide formation takes place<sup>332</sup>. However, firm theoretical evidence for this would have to come from simulations modelling subsurface adsorption and adsorption of atomic oxygen following DC, as well as bulk oxide formation. Such calculations, while certainly of high interest, would require a far larger scale, both in space and in time, than modelled here, and such a comparison is therefore outside the scope of this chapter.

Additionally, **Figure 5.4B** shows non-zero values of  $S_0$  (as seen in **Figure 5.3B**) for  $E_i^{\perp} < 5$  kJ/mol that, with the definitions we use, are attributed to trapping. The trapping probability we determined would strongly change had we used a different maximum propagation time. With a propagation time of 10 ps, it rises to 0.1, but its maximum decreases to about 0.02 for a maximum propagation

time of 100 ps, and to about 0.002 for the propagation time limit used here of 1 ns (see Figure 5.11 in Section 5.5.3). The observed trapping can thus be considered temporary. It is likely due to the physisorption of the O<sub>2</sub> molecule in the Van der Waals well observed in the elbows in Figure 5.2, as was also observed for the trapping of O<sub>2</sub> on Ag(111)<sup>162</sup>. In the relevant mechanism, the molecule is most likely trapped temporarily in the physisorption well due to energy transfer from the translational motion normal to the surface to parallel translational motion or the rotation of the molecule. As there is no mechanism for energy loss in the BOSS model, at some point, the energy flows back to the translational motion normal to the surface, and the molecule is desorbed. However, as also argued in Ref. <sup>162</sup>, the energy dissipation of the molecule needs to be modelled to describe trapping events properly. Energy dissipation of the molecule via interaction with surface atom motion is most likely 131,162,333 as electron-hole-pair excitations are less influential for larger diatomic molecules<sup>334</sup>. Trapping was not considered further here as how it proceeds here should largely be an artefact of the BOSS model used, and would not necessarily reflect reality.

The presence of the indirect mechanism for dissociation (as evident from Figure **5.4** for  $E_i^{\perp} > 22 \text{ kJ/mol}$ ) can be supported along similar lines as argued in Ref. <sup>319</sup> by a brief look at the PES, see Figure 5.2. Ramos et al. 319 showed that the indirect mechanism was driven by O<sub>2</sub> adsorbing parallel to the surface on the bridge site, as this has the lowest barrier for adsorption. After adsorption this precursor O<sub>2</sub> could move to the FCC site where it dissociates without a second barrier<sup>319</sup>. In our case, Figure 5.2 indicates that the FCC site does have a second barrier to dissociation. However, a rotation to  $\varphi = 90^{\circ}$  (see Section 5.2.1 and Figure 5.2E) on the bridge site seems to result in a path to reaction with only a low second barrier. We do reiterate that our grid in r may not be sufficiently large to investigate such a pathway in greater detail, as also discussed in Section 5.3.1, because the expansion of the r-grid would come at very high computational costs. It may be interesting to investigate the sticking with an extended r-grid when using a DF with a lower fraction of exact exchange admixed in the exchange-correlation DF. Because such a DF may yield better agreement with experiments, it could then be worth the additional computational resources to

expand the r-grid to exclude inaccuracy in the  $S_0$  due to the present use of a small grid.

It is interesting to study whether NES is maintained for dissociative chemisorption. As such, **Figure 5.5** presents the  $\Theta$  (incidence angle) dependent reaction probability for six different constant normal incidence energies. To keep the  $E_i^{\perp}$  constant the total incidence energy ( $E_i$ ) needs to increase for increasing  $\Theta$  such that

$$E_i^{\perp} = E_i \cos^2(\Theta) \tag{5.12}.$$

**Figure 5.5** shows to what extent NES of the total dissociation probability is obeyed for different values of  $E_i^{\perp}$ . At the lowest  $E_i^{\perp}$  for which non-zero results are shown ( $24 \, kJ/mol$ ), NES is not obeyed. This appears to be due to NES not being obeyed for indirect reactions, which is the dominant reaction mechanism for this  $E_i^{\perp}$ . At the highest  $E_i^{\perp}$  for which results are shown ( $\geq 72 \, kJ/mol$ ), NES is obeyed rather well. This appears to be due to NES being obeyed for direct dissociation, which is the dominant mechanism for these high  $E_i^{\perp}$ . At the intermediate  $E_i^{\perp}$  of  $48 \, kJ/mol$ , NES is also obeyed rather well, but now this appears to be due to opposing trends of indirect and direct reaction, with the indirect reaction probability decreasing and the direct reaction probability increasing with  $\Theta$ .

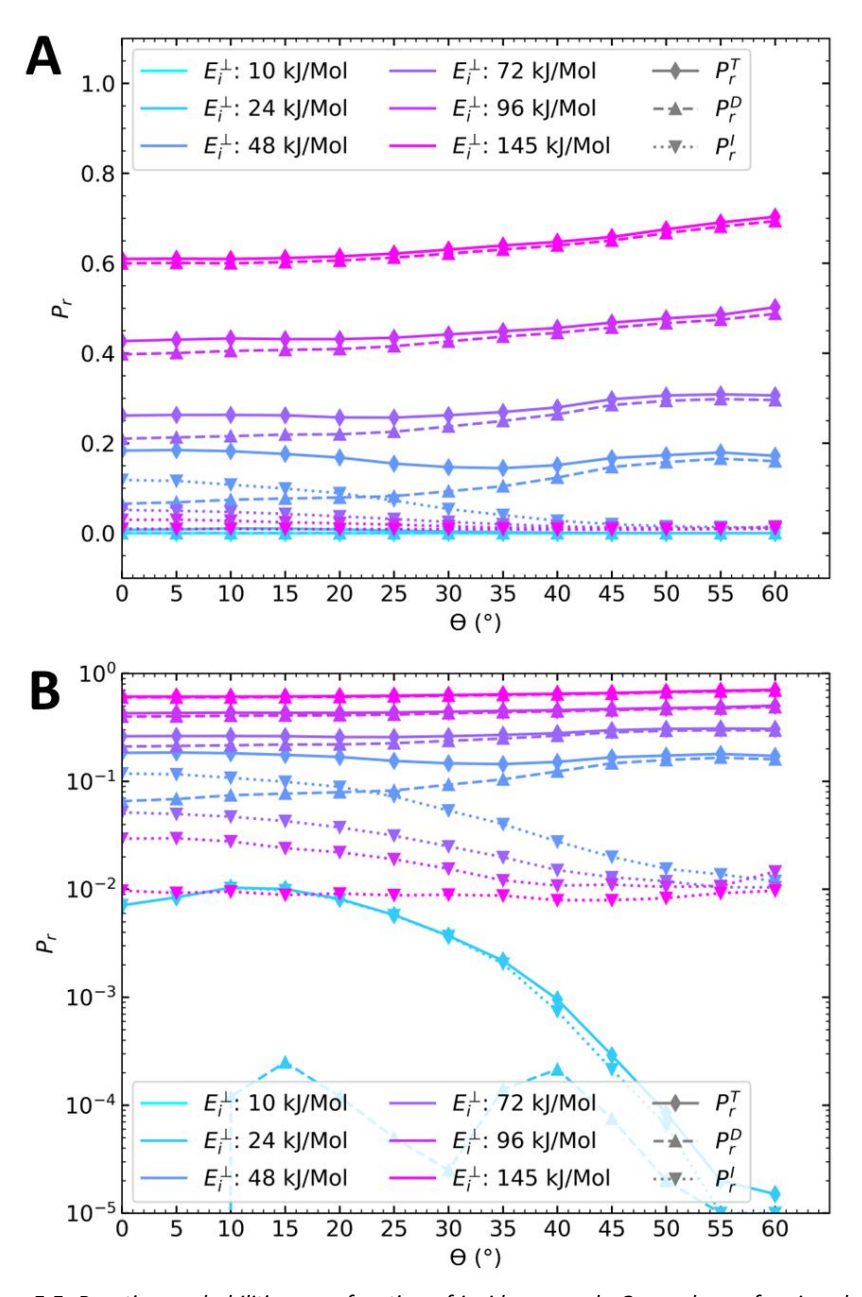


**Figure 5.5**: Reaction probabilities as a function of incidence angle  $\Theta$  are shown for six values of constant normal incidence energy  $(E_r^{\perp})$ ;  $P_r^{\top}$  is the total reaction probability,  $P_r^{D}$  is the direct reaction probability; **A**: reaction probability; **B**: Log plot of the reaction probability; **a** propagation time of 1 ns per trajectory was used, 200k trajectories were run per point.

#### 5.3.4 Discussion

To reiterate, the computed reaction probabilities for  $O_2 + Cu(111)$  using the HSE06-1/2x-vdWDF2 DF are the first DFT results that systematically underestimate the experimentally determined reaction probabilities. However, within the scope of the BOSS model, i.e., a O K static Cu(111) surface, this work also shows the possibility for both precursor-mediated dissociation as well as direct dissociation. The QCT results show that the incidence energy of  $O_2$  is a key factor in the interplay between these two mechanisms: the majority of the molecules with  $E_i^{\perp} < 53$  kJ/mol dissociate via a precursor state, but most of the molecules with  $E_i^{\perp} > 53$  kJ/mol dissociate directly. These results do not necessarily contradict the results and conclusions of Zhang  $et\ al.^{325}$ , as they explicitly stated that they could not rule out a transient, non-equilibrated molecular precursor with their experiments.

Some experiments have shown evidence for a molecular adsorbed O<sub>2</sub> species at  $T_{\rm S}$  < 160  $K^{\rm 322}$ , or indicate the possible presence of precursor-mediated dissociation for low  $T_5^{313,315}$ . These experiments are supported by previous theoretical work at the GGA level of theory that included  $T_S$  modelling<sup>319</sup>. Ramos et al. observed that for  $T_S = 100 \text{ K}$  most of  $S_0$  was non-dissociative<sup>319</sup>. We speculate based on the similarities in the shape of our PES (Section 5.3.1) and that of Ramos et al. 319 that for a PES based on the HSE06-1/2x-VdWDF2 DF, Ts may play a key role, similar to  $E_i^{\perp}$ , in the dissociation mechanism or type of  $S_0$ . Confirming this speculation would require  $T_s$  and atom surface motion to be included in the dynamics calculations. This would also be insightful for the possible trapping or physisorption at low  $E_i^{\perp}$  (Section 5.3.3).  $T_S$  and surface atom motion are also needed to reproduce the experimentally observed linear dependence of  $S_0$  on  $T_s^{325}$  and whether this linear dependency can be attributed to the recoil effect<sup>335</sup>, i.e., whether surface atom motion could help O<sub>2</sub> overcome the second barrier at higher T<sub>S</sub>, as proposed by both Hall et al.<sup>326</sup> and Zhang et al. 325. Therefore in future work  $T_S$  and surface atom motion need to be included for more definite conclusions on their influence on the sticking mechanisms.

Moving beyond a static surface can be difficult, especially with the already substantial computational costs involved in constructing the current static surface PES. A tried and tested method of including surface atom motion would

be to switch to a high dimensional neural-network (HDNN) PES<sup>123,303,336,337</sup>, which will allow for surface atom motion to be included in the PES. However, the training of such neural networks often requires large datasets and is a more serial process meaning that the computational expense of the hybrid HSE06-1/2x-VdWDF2 DF will make this a very time-demanding task. Another option could be the use of the GLO method, as Ramos  $et~al.^{319}$  did; this would not require any additional DFT calculations. Additionally, trying the dynamic corrugation (DCM) method, or if the sudden approximation were to be maintained the static corrugation (SCM) method, for modelling surface temperature may be an option, which was previously thoroughly and successfully tested for  $H_2 + Cu(111)^{109,110,159,160}$ .

Lastly, whilst using our current DF does not yield chemical accuracy, our results do suggest that a DF with high accuracy is within reach. The most obvious path forward is to reduce the fraction of exact exchange. As the work of Ramos et al. used a semi-local DF (i.e.,  $\alpha = 0$ ) and overestimated the reaction probabilities and this work ( $\alpha = 1/2$ ) underestimates the reaction probabilities, it seems that the truth may be somewhere in the middle. Ironically, it could turn out that the original HSE06 DF (with  $\alpha = 1/4$ ) will be a more accurate DF for this system. However, guessing the needed fraction of the exact exchange may result in a repetition of our current mistake. It may be necessary to scan more thoroughly for different allowed fractions of exact exchange  $(1/n, \text{ for } n = 2, 3, 4, 5, \text{ etc.})^{152}$  to test which one will result in the best agreement with the experiments. But we also note that scanning different fractions of exact exchange by constructing new PESs will be computationally very expensive at this moment. Thus, it may be fruitful to first test the accuracy of the non-self-consistent-field (NSCF) method as previously tested for  $O_2$  + Al(111)<sup>280</sup> (see Chapter 3). If this NSCF version produces results closely resembling the results of this chapter, it may be possible to scan across different fractions of exact exchange using the NSCF approach. Using the NSCF approach would dramatically reduce the computational costs of such a scan. From this scan, the ideal exact exchange fraction can then be estimated and used in the construction of a new fully self-consistent PES. The determination of this ideal fraction is best done in calculations also modelling  $T_s$ and surface atom motion. Otherwise agreement with experiment might come

from error cancellation, and the barrier height extracted from optimising the agreement with experiment could be incorrect.

# 5.4 Summary, conclusions, and outlook

This chapter presented the first implementation of a screened hybrid Van der Waals DF PES to quasi-classically model the sticking of  $O_2$  on Cu(111). The HSE06-1/2x-VdWDF2 DF was used to construct a 6D BOSS PES, using the CRP method to fit the DFT data. QCT calculations were performed using this PES to generate sticking probabilities for  $O_2$  + Cu(111) while simulating the experimental conditions of Zhang *et al.*<sup>325</sup>, also investigating the dependence of sticking on normal incidence energy and the angle of incidence. Furthermore, we were able to distinguish between different events in the QCT to disentangle contributions from trapping, direct, and indirect reactions.

The non-local HSE06-1/2x-VdWDF2 DF is the first DF to underestimate the sticking probability compared to experimental results. DFT studies based on semi-local GGA exchange (i.e. excluding exact exchange) always overestimated the sticking probability. This indicates that a similar screened hybrid DF with a lower fraction of exact exchange may exist that can describe the  $O_2 + Cu(111)$  dissociative chemisorption with high accuracy.

Moreover, this chapter shows evidence for the presence of two distinct mechanisms for dissociation. In our calculations, an indirect mechanism leads to dissociation of  $O_2$  when  $E_i^{\perp} > 22$  kJ/mol, becoming more important with an increase of the incidence energy up to  $E_i^{\perp} = 39.5$  kJ/mol, after which the probability of indirect reaction decreases. Meanwhile, the direct dissociative chemisorption starts to occur at  $E_i^{\perp} > 26$  kJ/mol, initially slowly but as the likelihood of the indirect mechanism decreases at higher incidence energies direct reaction eventually becomes the dominant mechanism for dissociation at  $E_i^{\perp} > 55$  kJ/mol. The interplay of the two mechanisms results in a plateau in the total reactivity of the system in the incidence energy range of 45 - 65 kJ/mol where the change of mechanism occurs from predominantly indirect to predominantly direct dissociation.

Lastly, in conjunction with other studies, this chapter suggests that the temperature of the Cu(111) surface may additionally play a key role in the interplay between the two possible mechanisms, as evidence for both has been readily found in literature but it is yet unclear which mechanism is dominant. However, the current study is unable to shine further light on the influence of surface temperature as this would require incorporating Cu surface atom motion into the PES. The computational costs of the BOSS-PES were already quite high so the proper modelling of the surface temperature effect at this level of DFT may prove challenging.

# 5.5 Appendices

The appendices contain three sections. In Section 5.5.1 the fitting of the  $O_2$  flux-weighted velocity distributions of the work of Zhang *et al.*<sup>325</sup> are presented and discussed. This section additionally presents both the resulting fitting parameters and the resulting average incidence energies. Section 5.5.2 presents one-dimensional potential energy "cuts" as a function of  $O_2$  above the surface for a constant bond length, showing the influence of molecular geometry on the Van der Waals well. Section 5.5.3 presents the log plot of the probabilities of the decoupled reactive events as a function of incidence energy of  $O_2$  for three different QCT propagation times.

# 5.5.1 Flux weighted velocity distribution fit

In the computation of sticking probabilities for comparison with supersonic molecular beam experiments, the molecular beam velocity distributions can be described by

$$N(V)dV = K_V V^3 e^{-\frac{(V - V_S)^2}{(\Delta V_S)^2}} dV$$
 (5.13),

where V is the velocity of the molecule,  $K_V$  is a normalisation constant,  $V_S$  is the stream velocity and  $\Delta V_S$  the width of the distribution width<sup>67</sup>. Additionally, the average velocity ( $V_{av}$ ) of the molecular beam can be defined as

$$V_{av} = \frac{\int V * N(V)dV}{\int N(V) dV}$$
 (5.14).

Similarly, the average energy of O<sub>2</sub> molecules in the beam can be computed using

$$E_{av} = \frac{\int \left(\frac{1}{2}m_{O2}V^2\right) * N(V)dV}{\int N(V)dV}$$
 (5.15),

where  $m_{O2}$  is the mass of the oxygen molecule.

The work of Zhang  $et~al.^{325}$  used four different  $O_2$  in He seeding ratios, resulting in four different velocity distributions. These four different velocity distributions were used in combination with different incidence angles to obtain  $S_0$  results for a range of different normal incidence energies. Below all four different distributions and the flux-weighted analytical distribution fits are plotted. The analytical fits are produced using a non-linear least squared fitting method, as implemented in the SciPy Python package. The integral for computing the average velocities and energies is based on the SciPy implementation of the quadpack fortran subroutine<sup>338</sup>.

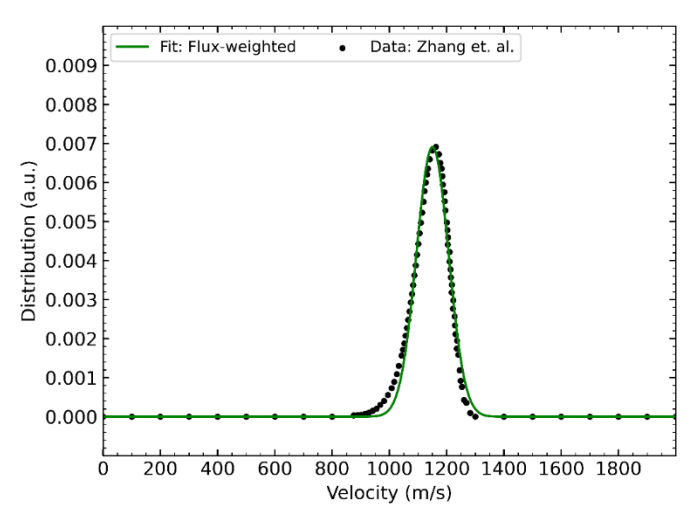


**Figure 5.6**:  $O_2$  molecular beam velocity distribution for the reported average incidence energy of 216 meV<sup>325</sup>. Black dots are the data as extracted from Ref. <sup>325</sup>, and green solid lines are the fluxweighted analytical distribution fits.

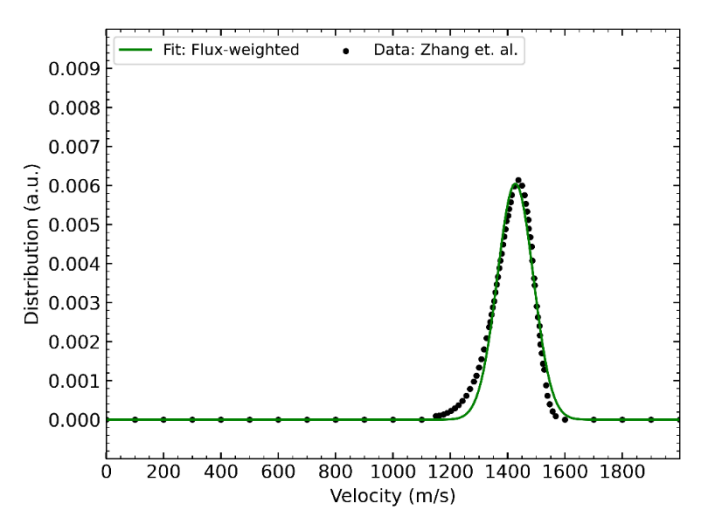


**Figure 5.7:**  $O_2$  molecular beam velocity distribution for the reported average incidence energy of 332 meV<sup>325</sup>. Black dots are the data as extracted from Ref. <sup>325</sup>, and green solid lines are the fluxweighted analytical distribution fits.

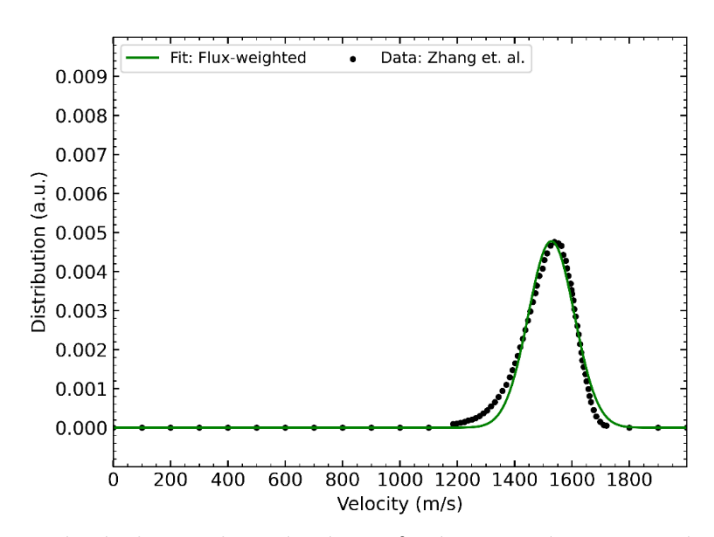


**Figure 5.8**:  $O_2$  molecular beam velocity distribution for the reported average incidence energy of 379 meV<sup>325</sup>. Black dots are the data as extracted from Ref. <sup>325</sup>, and green solid lines are the fluxweighted analytical distribution fits.

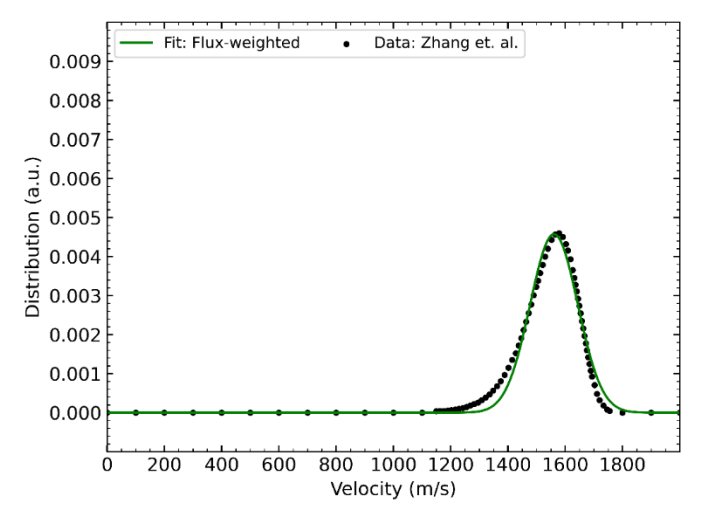


**Figure 5.9:**  $O_2$  molecular beam velocity distribution for the reported average incidence energy of 396 meV<sup>325</sup>. Black dots are the data as extracted from Ref. <sup>325</sup>, and green solid lines are the fluxweighted analytical distribution fits.

None of the four fits to the measured velocity distributions of Zhang *et al.*<sup>325</sup> are perfect. However, the average velocity and energy, peak velocity, and velocity width are all decently described by the flux-weighted fit. **Table 5.2** below shows all parameters of those fits that were used for our QCT dynamics.

**Table 5.2**: Comparison of the reported and fitted average energies of the molecular beam velocity distribution per experimental seeding ratio<sup>325</sup>. Additionally shown are the average velocities  $V_{av}$ , the fitted  $V_{sv}$   $\Delta V_{s}$  as used in the QCT dynamics, and the corresponding  $E_{s}$ , and  $\Delta E_{s}$ .

Seeding Ratios <sup>325</sup> O <sub>2</sub> /He	Reported  E <sub>av</sub> <sup>325</sup> (meV)	Fitted <i>E<sub>av</sub></i> ( <i>meV</i> )	Fitted $V_{av}$ ( $m/s$ )	Vs(m/s)	ΔVs (m/s)	Es (meV)	ΔEs (meV)
0.233	216	220.07	1150.65	1142.368	79.613	213	29.9
0.070	332	338.32	1426.98	1418.647	88.975	334	41.9
0.028	379	388.34	1528.21	1515.405	114.054	381	57.3
0.014	396	405.18	1560.92	1547.396	118.446	397	60.8

Furthermore, **Table 5.3** shows all the average normal incidence energies  $(E_i^{\perp})$  used as a result of varying the incidence angle  $\Theta$  such that:

$$E_i^{\perp} = E_i \cos{(\Theta)^2} \tag{5.16}.$$

**Table 5.3**: All normal incidence energies  $E_i^{\perp}$  in eV used per total incidence energy  $E_i$  (meV) and incidence angle  $\Theta$  in  $^{\circ}$ .

$E_i$ (meV)	<b>⊕</b> (°)	$E_{l}^{\perp}$ (eV)		
220.07	00	0.22007		
220.07	15	0.20533		
220.07	30	0.16505		
220.07	45	0.11004		
338.32	00	0.33832		
338.32	15	0.31566		
338.32	30	0.25374		
338.32	45	0.16916		
388.34	00	0.38834		
388.34	15	0.36233		
388.34	30	0.29126		
388.34	45	0.19417		
405.18	00	0.40518		
405.18	15	0.37804		
405.18	30	0.30389		
405.18	45	0.20259		

# 5.5.2 Physisorption, Van der Waals, well

The physisorption wells that most likely result from the Van der Wells (VdW) correlation are shown in **Figure 5.10** for different molecular geometries and a constant bond length. These results clearly show that the VdW-well is almost independent of the impact site of  $O_2$  on the surface for parallel orientations to the surface. However, the depth of the well is influenced by  $\theta$ , the polar orientation angle of the molecule. The well is shallower if the molecule is oriented along the surface normal, and for such orientations, the minimum of the well also occurs further away from the surface.

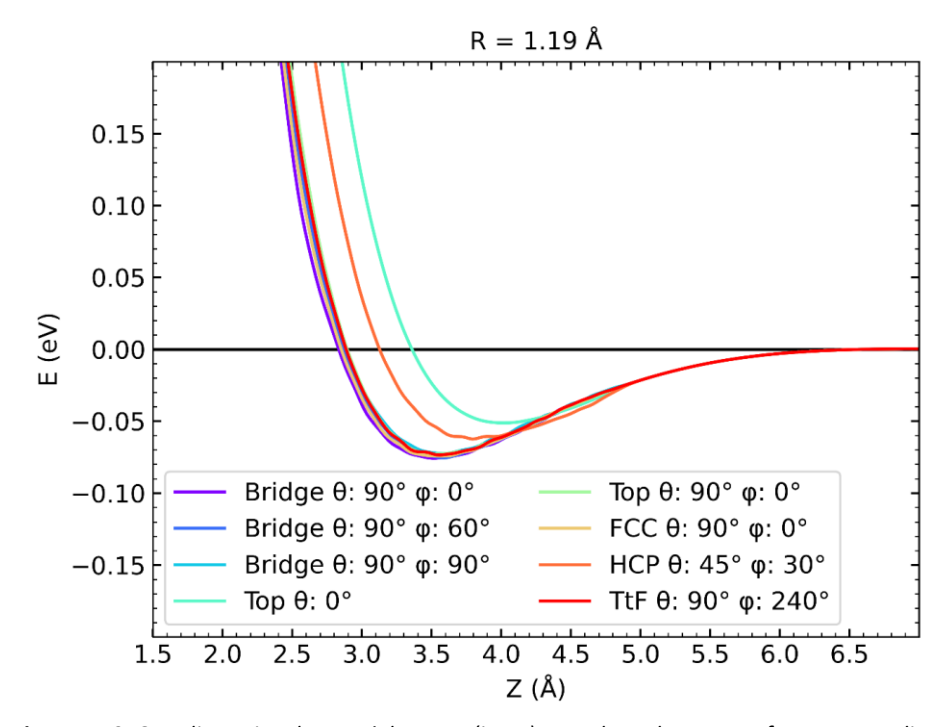


**Figure 5.10**: One-dimensional potential energy (in eV) cuts along the centre of mass Z-coordinate for an  $O_2$  bond length of 1.19 Å at different U, V-locations and for different molecular orientations  $(\theta, \varphi)$ .

# 5.5.3 Propagation-time dependent trapping

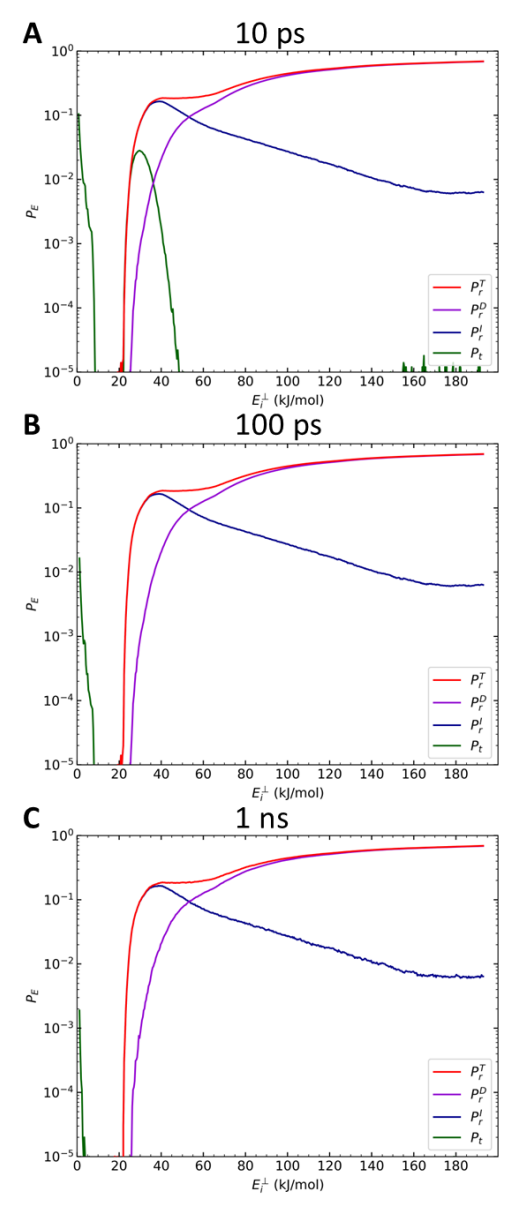


**Figure 5.11**: Log plot of the decoupled event probabilities as a function of normal incidence energy;  $P_r^T$  is the total reaction probability;  $P_r^D$  is the direct reaction probability;  $P_t^1$  is the indirect reaction probability;  $P_t$  is the trapping probability. Trajectories were run for every 4 meV (0.38 kJ/mol); **A**: 500k trajectories per  $E_r^A$ , propagation time of 10 ps; **B**: 500k trajectories per  $E_r^A$ , propagation time of 100 ps; **C**: 100k trajectories per  $E_r^A$ , propagation time of 1 ns.